Braz J Phys (2015) 45:699–707
DOI 10.1007/s13538-015-0354-7

SOCIEDADE BRASILEIRA DE FÍSICA

NUCLEAR PHYSICS

Study of the Elastic Scattering of ^{32}S by ^{24}Mg at Low Energies

Mahmoud A. Hassanain [1,2] · **Awad A. Ibraheem** [1,3]

Received: 8 July 2015 / Published online: 3 September 2015

Abstract The elastic scattering angular distribution of ^{32}S on ^{24}Mg at energies ranging from 65 to 110 MeV has been analyzed in the framework of the double folding (DF) model, using different effective nucleon-nucleon (NN) interactions based on the M3Y-Reid interaction. The Pauli correlation, zero-range, and finite-range exchange parts of the NN interactions are considered in the folding procedure to treat the single nucleon knock-on exchange term (SNKE) in the optical model. Successful reproduction of the data has been obtained with all the potentials considered in the present study. It is clear that the effect of Pauli correlation increases as the energy increases. Our calculations are insensitive to the strength of the imaginary potential used in the fit of the experimental data. We find also that the threshold anomaly is less pronounced in the ^{32}S + ^{24}Mg system. Our reaction cross sections are compared with the data, and the consistency between the real and imaginary volume integrals are checked by the dispersion relation.

Keywords Heavy-ion reactions · Pauli correlation · Knock-on exchange term · Volume integral

✉ Mahmoud A. Hassanain
mho1959@yahoo.com

[1] Department of Physics, King Khalid University, Abha, Saudi Arabia

[2] Physics Department, New-Valley Faculty of Science, El-Kharga, Assiut University, Assiut, Egypt

[3] Physics Department, Al-Azhar University, P.O. 71524, Assuit, Egypt

1 Introduction

During the last two decades or so, the double folding (DF) model for the real part of the optical potential was proved to give good description of heavy-ion (HI) elastic and inelastic scattering [1–7]. It expresses the potential in terms of the effective nucleon-nucleon interaction between the nucleons of the interacting nuclei, integrated over their densities. The M3Y effective NN interaction of Bertch et al [8], based on the G-matrix of the M3Y-Reid and M3Y-Pairs [9] has been widely used in the double folding model. Chamon et al. [10–13] have proposed an energy and density dependent real bare interaction for the description of a wide range of HI systems and energies. They obtained excellent fits to the data, especially in the refractive region. Farag et al. [14–16] have used two different approximate methods to treat the exchange term of the real M3Y potential to analyze the ^{16}O + ^{16}O, ^{16}O + ^{28}Si, and ^{32}S + ^{24}Mg collisions at 63, 142.5, and 110 MeV, respectively. The first prescription consists in adding to the M3Y effective NN interaction the pseudo-potential with a weak energy dependence. The second one consists in the folding of the M3Y effective NN potential with a two-body Pauli correlation function. They found that introducing the Pauli correlation function improves the agreement with the experimental data. EL-Azab Farid [17] has also used the α-cluster structure to compare with the M3Y potentials in the analysis of the ^{32}S + ^{24}Mg reaction in the energy range 65–110 MeV. He noticed that the predictions of the derived DFC potential are in better agreement with the data at backward angles (better than in the rainbow angles) for the two highest energies than those of the M3Y DF potential. The same data for ^{32}S + ^{24}Mg were measured and analyzed using the M3Y potentials by Pacheco et al. [18]. They found similar results using the microscopic and semi-phenomenological potentials at the two lowest incident

energies. In ref. [19], the elastic scattering of ^{32}S on ^{24}Mg, ^{27}Al, and ^{40}Ca were measured and analyzed using the phenomenological potential. Strong absorption radii have been extracted with and without consideration of the nuclear interaction at the surface. The relation between heavy-ion scattering and the saturation property with DDM3Y, BDM3Y, and CDM3Y was made clear by Dao T. Khoa and his collaborators [20–26].

Also, some previous [27–29] analyses of HI elastic scattering measurements have shown rapid variations with energy in the strengths of the nuclear optical potential in the vicinity of the coulomb barrier. There is a rapid increase in the absorptive strength, accompanied by a rapid decrease in the strength of the real potential, as the energy increases above the coulomb barrier. This effect has been referred to as a threshold anomaly. The effect has been observed to have weaker energy dependences for ^{32}S + ^{32}S [27, 28] and ^{32}S + ^{40}Ca [29]. In order to extend the studies of this reaction, we have investigated the elastic scattering of ^{32}S on ^{24}Mg, in the framework of the double folding model with the M3Y-Reid NN interactions, with their exchange parts divided into the Pauli correlation function, the zero-range, and the finite-range interactions [14–17, 30, 31]. Five sets of ^{32}S + ^{24}Mg elastic scattering data were analyzed over the energy range 65–110 MeV. In the following section, the theoretical formalism is presented, while our procedure is explained in section 3. Section 4 is devoted to results and discussions and finally the conclusions are summarized in section 5.

2 Theoretical Formalism

2.1 Folding Approaches

Our aim in the present study is to analyze of the elastic scattering of the ^{32}S + ^{24}Mg in the framework of DF model by using three different approximation methods to treat the exchange part in real M3Y potential. The first prescription consists in adding to the real M3Y-Reid effective NN interactions a knock-on exchange term to account for the one pion exchange potential (OPEP) in the finite-range forms [32, 33]. In order to compare easily, we refer to these potentials as CDM3Y6-FR and DDM3Y-FR. Also, we replacing the nondiagonal density $\rho\left(\vec{r},\vec{r}'\right)$ appearing in the exchange part of the optical potentials by an approximation based on the density matrix expansion (DME) used the iteration procedure [20, 21, 23, 24, 30, 31]. While the second one is obtained by adding to the real M3Y-Reid effective NN interaction as pseudo-potential with weak energy dependence in zero-range form. These potentials refer to DDM3Y-ZR and M3Y-ZR [17, 34]. The last method, denoted as M3Y-P, is obtained as a folding of the density-independent M3Y-Reid effective interaction potential with a two-body Pauli correlation function [14–16, 35, 36].

The real part of the complex nuclear potential is determined by using the DF model. In order to obtain the double folding potential, the nuclear matter density distribution of both projectile and target nuclei together with an effective nucleon-nucleon interaction potential $V_{NN}(s)$ are used. In the first order of Feshbach's theory for the optical potential, the projectile-target potential can be evaluated as a Hartree-Fock (HF) type potential for the dinuclear system.

$$V_{\mathrm{DF}} = V_D + V_{\mathrm{EX}} = \sum_{i\in A_p, j\in A_T} [\langle ij|V_D|ij\rangle + \langle ij|V_{\mathrm{EX}}|ij\rangle], \quad (1)$$

Where $|i\rangle$ and $|j\rangle$ refer to the single particle wave functions of the nucleon in the two colliding nuclei, while V_D and V_{EX} are, respectively, the direct and exchange parts of HI potential.

The direct potential $V_D(E,R)$ is obtained by using the usual folding method [7]:

$$V_D(E,R) = \int \rho_P\left(\vec{r}_P\right)\rho_T\left(\vec{r}_T\right)V_D(\rho,E,s)d\vec{r}_P d\vec{r}_T \quad (2)$$
$$\vec{s} = \vec{R} + \vec{r}_T - \vec{r}_P;$$

where $\rho_P(r_P)$ and $\rho_T(r_T)$ are the densities for the projectile and target nuclei. R is the separation of the center-of-mass of the target and projectile and s is the distance between their nucleons.

The exchange potential $V_{\mathrm{EX}}(E,R)$ is calculated within a generalized version of the double folding model [20, 21].

$$V_{\mathrm{EX}}(E,R) = \int \rho_P\left(\vec{r}_P,\vec{r}_P+\vec{s}\right)\rho_T\left(\vec{r}_T,\vec{r}_T-\vec{s}\right) \quad (3)$$
$$\times V_{\mathrm{EX}}(\rho,E,S)\exp\left[\frac{i\vec{k}(R).\vec{s}}{\mu}\right]d\vec{r}_P d\vec{r}_T$$

Here, $k(R)$ is the relative-motion momentum given by

$$K^2(R) = \frac{2m\mu}{\hbar^2}[E_{\mathrm{c.m.}} - V_{\mathrm{DF}}(E,R) - V_C(R)] \quad (4)$$

where μ is the reduced mass, $\mu = A_P A_T/(A_P+A_T)$ with A_P and A_T as the mass numbers of the projectile and target, respectively, $E_{\mathrm{c.m.}}$ is the relative energy in the center-of-mass system, and m is the bare nucleon mass. In Eq. (4), $V_{\mathrm{DF}}(E,R) = V_D(E,R) + V_{\mathrm{EX}}(E,R)$ is the total nuclear potential and $V_C(R)$ is the coulomb potential. Here, we choose the conventional point-like plus uniform charge model to calculate the coulomb potential. In order to simplify the numerical calculation of $V_{\mathrm{EX}}(E,R)$, many authors [20–22, 30, 31, 37] have used an approximate [38] for the density matrix derived from the DME method [39]. This approximation is

$$\rho\left(\vec{R},\vec{R}+\vec{S}\right)=\rho\left(\vec{R}+\frac{\vec{S}}{2}\right)\hat{j}_1\left[K_{\text{eff}}\left(\left|\vec{R}+\frac{\vec{S}}{2}\right|\right)S\right],$$

$$\text{where}\qquad \left|K^i_{\text{eff}}(r)\right|^2=\frac{5}{3\rho(r)}\left[\tau(r)-\frac{1}{4}\nabla^2\rho(r)\right],$$

$$\text{and}\qquad \hat{j}_1(x)=\frac{3}{x}j_1(x)=3\,\frac{\sin x-x\cos x}{x^2} \tag{5}$$

Where $\hat{j}_1(x)$ is the first-order spherical Bessel function. For a spherically symmetric ground state density, the average local Fermi approximation, $K_{\text{eff}}(i=P,T)$, is given in terms of the kinetic energy density $\tau(r)$ as [38]. Usually, $\tau(r)$ is calculated using one of the two approximations

$$\tau(r)=\frac{3}{5}K_f^2\rho(r)+\frac{1}{3}\nabla^2\rho(r)+\frac{1}{36}\frac{[\nabla\rho(r)]^2}{\rho(r)}, \tag{6a}$$

$$\text{and}\quad \tau(r)=\frac{3}{5}K_f^2\rho(r)+\frac{1}{3}\nabla^2\rho(r)+\frac{1}{4}\frac{[\nabla\rho(r)]^2}{\rho(r)}, \tag{6b}$$

Where the first term in each approximation is the Thomas-Fermi term with

$$K_f^2=\left[\frac{3}{5}\pi^2\rho(r)\right]^{2/3}$$

The two equations, Eqs. (6a) and (6b), are derived from the extended Thomas-Fermi approximation which is given by

$$\tau(r)=\frac{3}{5}K_f^2\rho(r)+\frac{1}{3}\nabla^2\rho(r)+\frac{C_s[\nabla\rho(r)]^2}{\rho(r)}$$

The third term is the so-called Weizsacher term with strength C_s. It represents the contribution of $\tau(r)$ form the surface of the nucleus. Normally, one takes $C_s=\frac{1}{36}$ for the finite fermionic system, many authors [40–43] have used this value with ordinary M3Y forces to drive the real optical potential. So, assuming the local approximation Eq. (5) and using the energy and density dependent exchange interaction Eq. (3), one easily obtains the self-consistent and local exchange potential V_{EX} as

$$V_{\text{EX}}(E,R)=4\pi g(E)\int_0^\infty v_{\text{EX}}(s)j_0\left(K\left(\vec{R}\right)s/M\right)s^2ds \times\int f_P\left(\vec{r},s\right)f_T\left(\left|\vec{r}-\vec{R}\right|,s\right)F\left[\rho_p\left(\vec{r}\right)+\rho_2\left(\vec{r}-\vec{R}\right)\right]d^3r \tag{7}$$

Where

$$f_{P(T)}\left(\vec{r},s\right)=\rho_{P(T)}\left(\vec{r}\right)\hat{j}_1\left(K_{F_{P(T)}}\left(\vec{r}\right)s\right)\text{ and }\hat{j}_0(x)=\frac{\sin x}{x} \tag{8}$$

The exchange potential Eq. (7) can then be evaluated by the iteration procedure [20, 21]. For NN interactions $V_{D(\text{EX})}(\rho,E,s)$ in Eqs. (2) and (3) are the so-called density- and energy-dependent NN interactions. They are given by refs. [20, 21],

$$V_{D(\text{EX})}(\rho,E,s)=F(\rho)g(E)V_{D(\text{EX})}(s), \tag{9}$$

where $V_{D(\text{EX})}(s)$ are the so-called M3Y-Reid interactions. The M3Y-Reid direct part is

$$V_D(s)=7999\frac{\exp(-4s)}{4s}-2134\frac{\exp(-2.5s)}{2.5s} \tag{10}$$

and the M3Y-Reid knock-on exchange parts in the finite-range exchanges is

$$V_{\text{EX}}(s)=4631\frac{\exp(-4s)}{4s}-1787\frac{\exp(-2.5s)}{2.5s}-7.847\frac{\exp(-0.7072s)}{0.7072s} \tag{11}$$

and

$$F(\rho)=C[1+\alpha\exp(-\beta\rho)-\gamma\rho] \tag{12}$$

The overlap density ρ in $F(\rho)$ is usually taken to be the sum of projectile and target densities ($\rho=\rho_P+\rho_T$) for the direct potential. In the case of exchange potential Eq. (3), the overlap density ρ is the total density at the midpoint between the two nucleons being exchanged,

$$\rho=\rho_P\left(\vec{r}_P+\frac{\vec{s}}{2}\right)+\rho_T\left(\vec{r}_T-\frac{\vec{s}}{2}\right) \tag{13}$$

and $g(E)$ in Eq. (9) is given by

$$g(E)=\left[1-G\frac{E}{A_P}\right] \tag{14}$$

In the M3Y-Reid versions (DDM3Y-FR and CDM3Y6-FR), G in Eq. (14) is equal to 0.002 MeV^{-1}. The corresponding values for C, α, β, and γ for the two versions DDM3Y-FR and CDM3Y6-FR interactions were chosen to reproduce the required saturation properties are collected in Table 1 together with the predicted incompressibilities K [20, 21, 23, 24].

In the present work, as above discussed, we will use three different approximation methods to treat the exchange term in real M3Y-Reid effective interactions. The first prescription method of calculating the real part of the optical potentials (DDM3Y-FR and CDM3Y6-FR) could be given by introducing Eq. (9) into Eqs. (2) and (7). While the second one is obtained by adding to the real DDM3Y effective interaction the zero-range pseudo-potential with weak energy

Table 1 The coefficients of the different density-dependent NN interactions

Interaction	C	α	β (fm^3)	γ (fm^3)	K (MeV)
DDM3Y-FR	0.2843	3.6391	2.9605	0.0	171
CDM3Y6-FR	0.2658	3.8033	1.4099	4.0	252

dependence to represent the knock-on exchange (DDM3Y-ZR). The result can be expressed as

$$J_{00}(E) = -276[1-0.005E_{\rm lab}/A_P] \quad \text{MeV fm}^3 \tag{15}$$

Where, $E_{\rm lab}$ is the laboratory energy of the projectile. Also, Eq. (12) can be rewritten as dependent of the laboratory energy of the projectile for the DDM3Y-ZR version potential [34, 44, 45]

$$F(E,\rho) = C(E)[1+\alpha(E)\exp(-\beta(E)\rho) \tag{16}$$

The energy-dependent parameters of Eq. (16) are taken from ref. [34], while for M3Y-ZR DF potential, we use only Eqs. (10) and (15) into Eq. (2) without density dependent.

The third method is obtained as a folding of the direct M3Y-Reid NN interaction potential with a two-body Pauli correlation function (M3Y-P). The Pauli principle implies that the total wave function for the colliding nuclei be antisymmetric under interchange of nucleons between the two colliding nuclei. So, the general form for the double-folding optical potential model by inserting the Pauli correlation effect is given by [14–16]

$$V_{\rm DF}(R) = \int dr_T \rho_T(r_T) \int dr_P \rho_P(r_P) V_{NN}(s)[1-\zeta(s)] \tag{17}$$

Where $\zeta(s)$ is the two-body Pauli correlation function and is given in the Fermi-gas model [40–43] by the expression

$$\zeta(s) = \frac{1}{4}\exp\left(-0.1K_F^2 s^2\right), \tag{18}$$

Where K_F is the Fermi wave number and is taken to be 1.36 fm^{-1}. By introducing Eqs. (10) and (18) into Eq. (17), it represents the third prescription of calculating the real part of the optical model potential with Pauli correlation effect (M3Y-P).

The real folding potential $V_{\rm DF}(E,R)$ must be supplemented by the imaginary potential. So, the imaginary potential has been taken as a standard Woods-Saxon (WS) form:

$$W(R) = \frac{W_0}{1+\exp((R-r_I)/a_I)} \tag{19}$$

and the total local potential $U(R)$ is written

$$U(E,R) = V_C(R) + N_R V_{DF}(E,R) + iW(R) \tag{20}$$

Where N_R is the normalization factor of the real potential, and $W(R)$ is the imaginary part. The depth W_0, the radius r_I, the diffuseness a_I, and the renormalization factor N_R can be adjusted in order to reproduce fit data.

2.1.1 The Density Distributions

The charge densities distribution for the projectile and target were taken from electron-scattering data [18] in the parameterized Fermi parabolic form,

$$\rho(r_i) = \rho_{Oi}\left(1+w\left(\frac{r}{c}\right)^2\right)/\left(1+\exp\left(\frac{r-c}{a}\right)\right),\ i=P,T \tag{21}$$

In Table 2, we include the values of these parameters for the system analyzed. The ρ_{Oi} values were obtained by normalizing to the nuclear masses.

3 Procedure

We have analyzed the elastic scattering of ^{32}S + ^{24}Mg over energy range 65–110 MeV within the framework of the double folding model. The direct term in the DF approach is supplemented with an exchange term given in the expressions (3), (15), and (18). We introduced the central real DF potentials given by our computer code [46] and DFPD4 computer code [47] into HI-OPTIM-94 [48] computer program, the angular distribution of differential cross sections are calculated. Searches were carried out by optimizing four free parameters, the real renormalization factor N_R for the calculated potentials besides the three parameters of the imaginary phenomenological WS potentials, the depth W_0, radius r_I, and diffuseness a_I in order to fit the data by minimizing the χ^2 parameter.

4 Results and Discussion

In the present work, five sets of data for the differential cross section of ^{32}S + ^{24}Mg elastic scattering at energies around and above the barrier, $E_{\rm lab}$=65, 75, 86, 95.07, and 110 MeV, are analyzed using five versions from M3Y NN interaction in the optical model potentials (M3Y-ZR, DDM3Y-ZR, DDM3Y-FR, CDM3Y6-FR, and M3Y-P). The obtained parameters and associated real and imaginary volume integrals per

Table 2 Values of the ρ_{Oi}, w, C, and a parameters and the corresponding rms radii for the ^{23}S and ^{24}Mg nuclei used in Eq. (21)

Nucleus	ρ_{Oi} (fm^{-3})	w	C (fm)	a (fm)	$\langle r^2\rangle^{1/2}$ (fm)
^{24}Mg	0.1789	−0.249	3.192	0.604	2.961
^{32}S	0.1825	−0.213	3.441	0.624	3.224

interacting nucleon-pair, J_R, J_I in addition to the resulted reaction cross sections, σ_R, are listed in Table 3 and the corresponding fits with experimental data are shown in Fig. 1. Only the real and imaginary volume integrals, J_R, J_I of both DDM3Y-ZR and M3Y-P potentials are displayed in Figs. 3 and 4 in comparison with the dispersion relation curve.

The angular distributions of the $^{32}S + ^{24}Mg$ elastic scattering are calculated for five versions at different bombarding energies are shown in Fig. 1. From this figure, it is found that using the effective NN interaction with Pauli correlation function gives agreement with the experimental data similar or better than that the other different versions used in this work with N_R close to unit value approximately.

The shapes of the potentials used in our calculations are shown in Fig. 2 only at the highest three energies (E_{lab}=86, 95.1, and 110 MeV). We observe from this figure that all real potentials have the same strength and slope at the surface which corresponds to the small overlap or low-density region. The main difference between different types of the folded potential is showing up at small inter-nuclear distances which correspond to the higher overlap density of the two colliding nuclei. In Fig. 2, we also show the folding potential calculated using the density independent interaction (M3Y-ZR) is deeper than M3Y-P potential especially at small radii, while the other DF microscopic potentials (DDM3Y-ZR, DDM3Y-FR, and CDM3Y6-FR) are quite close resemblance to each other and to the M3Y-P potential in the entire radial range in most considered energies. The corresponding imaginary potentials are weak (shallow depth) and quite close to each other for all considered energies.

According to these results, the values of the volume integral in Table 3 are also different. We notice that the real volume integral values, J_R, for M3Y-P interaction smaller than the values of the volume integral obtained by the other interactions we have considered in this paper. In order to check consistency between the real and imaginary parts, we have applied the dispersion relation to the values of the real and imaginary volume integral. The volume integral of the real and imaginary potentials and the dispersion relation [49] between them have been calculated by using the following formula

Table 3 The optical potential parameters and χ^2 values obtained used in our double folding model analyses of the elastic $^{32}S + ^{24}Mg$ scattering data at E_{lab}=65–110 MeV

Energy (MeV)	Potential	N_R	W_0 (MeV)	r_w (fm)	a_w (fm)	J_R (MeV fm^3)	J_I (MeV fm^3)	σ_R (mb)	χ^2
65	M3Y-ZR	0.96	4.844	1.305	0.365	403.9	13.34	45.62	0.3
	DDM3Y-ZR	0.60	4.620	1.305	0.430	206.9	12.48	46.19	0.4
	DDM3Y-FR	0.66	4.620	1.305	0.426	290.8	12.81	49.68	0.3
	CDM3Y6-FR	0.74	5.028	1.348	0.273	309.8	15.12	45.36	0.3
	M3Y-P	1.01	4.620	1.384	0.455	146.1	15.29	59.22	0.7
75	M3Y-ZR	0.96	4.945	1.463	0.326	402.5	26.74	434.0	0.2
	DDM3Y-ZR	0.60	5.197	1.487	0.296	206.0	20.94	424.4	0.2
	DDM3Y-FR	0.73	6.855	1.467	0.304	320.5	26.56	429.2	0.2
	CDM3Y6-FR	0.73	6.360	1.472	0.310	305.4	24.92	431.6	0.2
	M3Y-P	1.06	6.200	1.478	0.411	153.4	24.81	480.0	0.3
86	M3Y-ZR	0.97	6.971	1.411	0.397	407.1	24.25	737.4	1.1
	DDM3Y-ZR	0.57	7.620	1.391	0.418	194.3	25.48	719.9	1.4
	DDM3Y-FR	0.65	7.620	1.386	0.396	283.5	25.21	708.3	1.3
	CDM3Y6-FR	0.68	7.640	1.393	0.395	286.7	25.60	717.8	1.3
	M3Y-P	1.09	7.301	1.436	0.503	157.7	27.10	839.8	2.4
95.07	M3Y-ZR	0.97	12.463	1.339	0.490	405.7	37.59	974.8	1.9
	DDM3Y-ZR	0.54	10.485	1.342	0.515	181.5	31.97	961.0	1.8
	DDM3Y-FR	0.56	12.685	1.311	0.547	243.5	36.31	970.8	1.8
	CDM3Y6-FR	0.56	12.685	1.310	0.560	234.0	36.33	982.0	1.8
	M3Y-P	1.04	10.060	1.349	0.594	150.5	31.52	1036	2.0
	M3Y-P	1.02	72.451	1.096	0.669	147.6	127.2	1064	1.9
110	M3Y-ZR	0.99	12.343	1.292	0.562	412.5	33.91	1226	6.6
	DDM3Y-ZR	0.53	9.066	1.321	0.615	175.7	26.82	1251	7.2
	DDM3Y-FR	0.53	11.792	1.245	0.622	229.4	29.48	1175	5.1
	CDM3Y6-FR	0.56	12.022	1.248	0.603	232.9	30.14	1166	5.1
	M3Y-P	0.98	11.002	1.348	0.665	141.8	28.14	1188	5.2

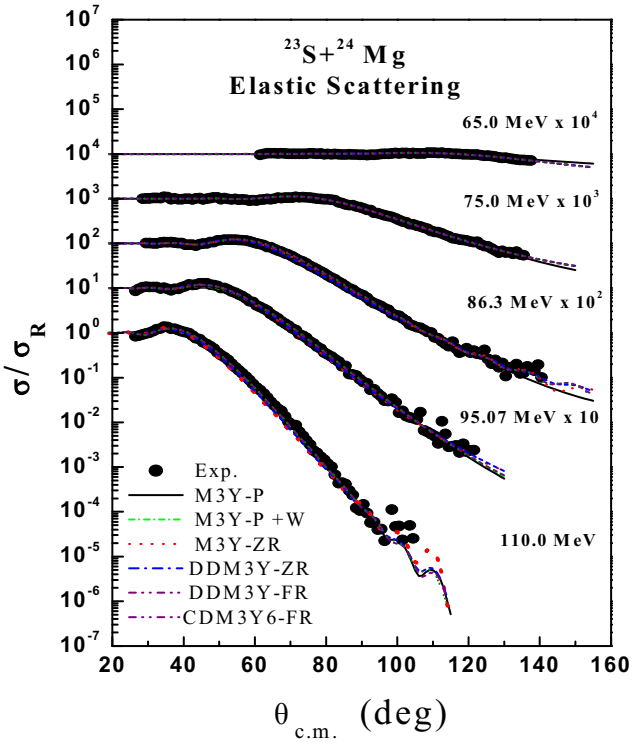

Fig. 1 A comparison between the measured ^{23}S + ^{24}Mg scattering differential cross sections and theoretical predictions obtained by using the M3Y-P, M3Y-ZR, DDM3Y-ZR, DDM3Y-FR, and CDM3Y6-FR at energies of 65, 75, 86, 95.07, and 110 MeV. Data are taken from refs. [17, 18]

$$J_{R,I}(E) = \frac{4\pi}{A_P A_T}\int_0^R V, W(r,E)r^2 dr, \tag{22}$$

$$V_N(E) = V_R + \Delta V(E) = V_R - (W/\pi)[\varepsilon_a \ln|\varepsilon_a| - \varepsilon_b \ln|\varepsilon_b|] \tag{23}$$

Here, $\varepsilon_i=(E-E_i)/(E_b-E_a)$ with i as a and b, respectively. The E_a energy is assumed to be the value at which the imaginary potential vanishes and E_b is the reference energy. The parameters are E_a=45 MeV and E_b=86 MeV, V_R=153 (194)MeV, and W_0=27 MeV for both M3Y-P and DDM3Y-ZR potentials, respectively. The volume integrals for the real and imaginary parts of both M3Y-P and DDM3Y-ZR potentials are shown in Figs. 3 and 4. We can notice from these figures that the real volume integrals of both M3Y-P and DDM3Y-ZR potentials have clear energy dependence, where J_R decreases as energy increases obey the dispersion relation curve. While, the imaginary volume integral strength J_I increases rapidly follow the trend of the dispersion relation curve. Comparing our results with those obtained by previous studies, we found that our results have an equal success as that obtained by the microscopic analysis using the DFC by El-Azab Farid [17] with the same data. Also, we found that the present fits are better than those obtained by refs. [14–16] at the energy 110 MeV and are quite satisfactory and sometimes better than those obtained by ref. [18].

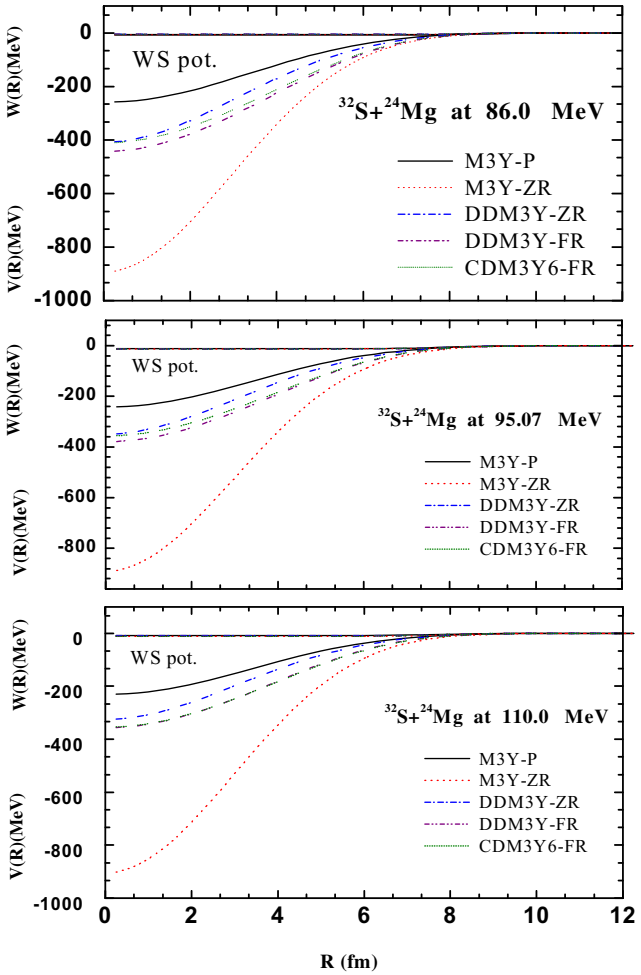

Fig. 2 The comparison of the radial shapes of the real microscopic nuclear potentials (M3Y-P, M3Y-ZR, DDM3Y-ZR, DDM3Y-FR, and CDM3Y6-FR) and volume woods-Saxon (WS) imaginary potential used in our calculations at E_{lab}=86, 95.07, and 110 MeV

It has been mentioned in refs. [17, 18] that the results are insensitive to strength parameters of the imaginary potential at near- and sub-barrier energies for ^{32}S + ^{24}Mg. In order to observe whether the strength parameter of the imaginary potential has an effect on the results, we have conducted a new calculation with one set of energy by using the M3Y-P potential with the Pauli correlation effect with the same parameters as in Table 3. The short dash dot line in Fig. 1 at E_{lab}=95.07 MeV is the result of the calculations with W_0=72.451 MeV. The other parameters are listed in Table 3. As it can be perceived from this figure, the results are insensitive to the strength of the imaginary potential for this interaction. This indicates, as mentioned in refs. [17, 18] that the absorption takes place on the same region of the nuclear surface independently of the strength W_0.

From Table 3, we should also point out here that the renormalization factor N_R for DDM3Y-ZR, DDM3Y-FR, and DDM3Y6-FR has slightly clear energy dependence, where N_R slightly decreases as energy increases, except in M3Y-ZR and M3Y-P interactions, the values of N_R are close

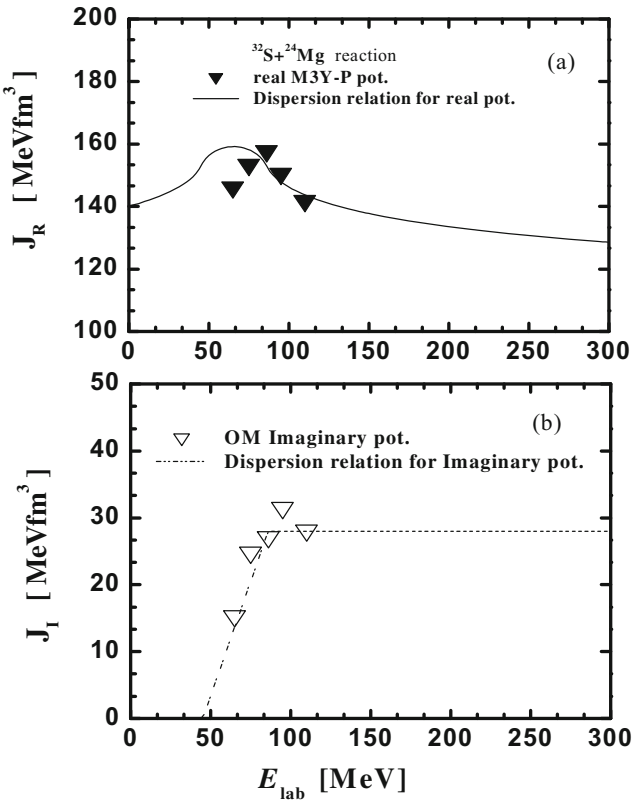

Fig. 3 Volume integrals for the potentials found in this study. *Full* and *empty triangles* result from the M3Y-P effective interaction and the *solid* and the *dashed lines* are the dispersion relation between real and imaginary components of the nuclear potential calculated by Eq. (23)

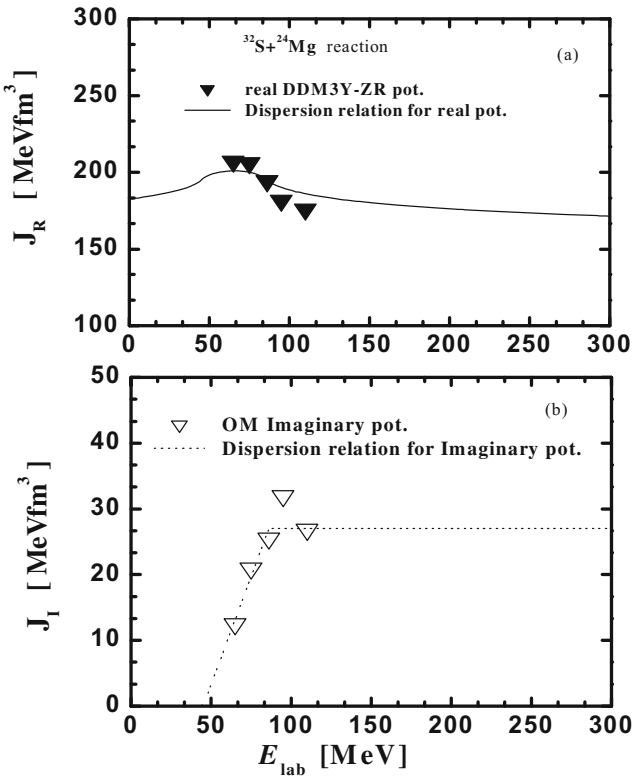

Fig. 4 The same as Fig. 3 but *full* and *empty triangles* result from the DDM3Y-ZR interaction

to unit value approximately. In Fig. 5, values for the renormalizations factor N_R are plotted against the energy. From this figure, it is evident that the renormalization factor N_R obtained from the analysis of the ^{32}S + ^{24}Mg reaction by using the DDM3Y-ZR potential has slightly decreases as energy increases with the energy dependence factor~(0.73–0.002 E_{lab}). The same behavior for the renormalization factor N_R for M3Y-P potential as display in the same figure, where N_R slightly decreases as energy increases with the energy dependence factor~(1.104–0.008 E_{lab}), it has been close to the unit (N_R= 1). These results are agreed with that the phenomenon, known as the threshold anomaly, was observed in the scattering of different systems [23–25]. It arises from the coupling between the elastic and inelastic channels. Our results obtained by DDM3Y-ZR, DDM3Y-FR, and CDM3Y6-FR potentials are consistent with that noticed for the renormalization of the DFC and M3Y DF potentials [17, 18] obtained from the analysis of the ^{32}S + ^{24}Mg reaction at the same energies.

From this analysis, we can see that one density-dependent effect is not important in the differential cross-section calculations, when it included with the zero-range exchange, but the situation to fit the data is different with the finite-range exchange.

Also, we notice that introducing the finite-range exchange in the two versions for density dependent for the M3Y effective interaction through the DF potentials (DDM3Y-FR and CDM3Y6-FR) yields improvement in fitting with data than the other prescription. This may indicate that the effect of finite exchange observe at low energy with HI interactions. At the same time, the effect of Pauli correlation observe when the energy of projectile increases. Also, the results from the M3Y-P DF potential are insensitive to the strength of the imaginary potential for all consider energies.

For completeness, we display in Fig. 6 energy dependence of the total reaction cross-section σ_R obtained from the present

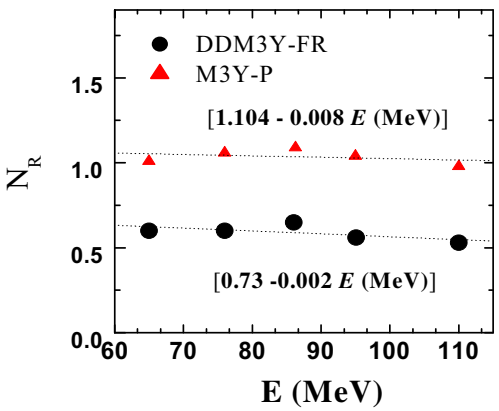

Fig. 5 The energy dependence with the normalization coefficient, N_R deduced from the analysis of ^{32}S + ^{24}Mg elastic scattering using the DDM3Y-FR and M3Y-P interactions; *dash lines* are drawn to guide eyes

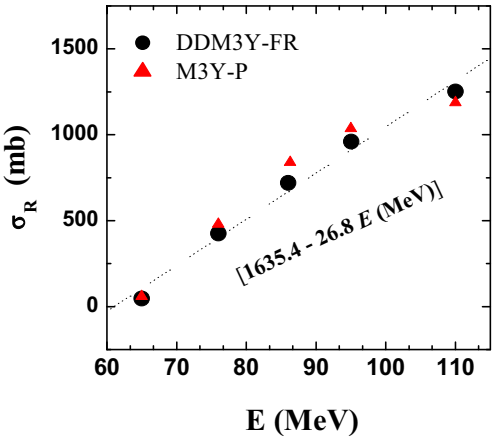

Fig. 6 The energy dependence of the total reaction cross section, σ_R deduced from the analysis of $^{32}S + ^{24}Mg$ elastic scattering by using the DDM3Y-ZR and M3Y-P interactions; *dash lines* are drawn to guide eyes

analysis by DDM3Y-ZR and M3Y-P interactions. As clearly noticed, from Table 3, the results from all considered potentials are identical and have linear energy dependence. We find $\sigma_R = C + DE$, where $C = 1635.4$ mb and $D = -26.8$ for DDM3Y-ZR and M3Y-P potentials, i.e., the energy dependence in the all potentials have slightly different slopes ~28. It is clear that at near-barrier energies, the total reaction cross section is very small because it takes place at the nuclear surface in a very narrow domain; this domain broadens with increasing energy and consequently σ_R increases [17]. On the other hand, our results are slightly higher than those yielded by microscopic M3Y DF and DFC potentials for $^{32}S + ^{24}Mg$ [17, 18]. Finally, we can say that the dispersion between the different values of σ_R is close to 8 % [22].

5 Conclusion

In the present study, the effective NN interactions are divided into density- independent and density-dependent NN interactions, based on the M3Y-Reid NN interaction. The exchange parts were divided into the Pauli correlation effect, the zero-range, and the finite-range interactions. In order to compare easily, we denote the Pauli correlation effect and density-independent and density-dependent zero-range interactions by M3Y-P, M3Y-ZR, and DDM3Y-ZR NN, while the density-dependent finite-range interactions are DDM3Y-FR and CDM3Y6-FR NN interactions. Also, we are replacing the nondiagonal density $\rho\left(\vec{r}, \vec{r}'\right)$ appearing in the exchange part of the optical potentials by an approximation based on the density matrix expansion (DME) used the iteration procedure in DDM3Y-FR and CDM3Y6-FR NN interactions.

Five sets of $^{32}S + ^{24}Mg$ elastic scattering angular distributions data at laboratory energies ranging from 65 to 110 MeV were analyzed using the derived potentials. The results of our calculations with all the different versions of the M3Y NN interaction potentials used (DDM3Y-FR, CDM3Y6-FR, DDM3Y-ZR, M3Y and M3Y-P) yielded qualitatively consistent results approximately. We noted that the results obtained using the DDM3Y-FR and CDM3Y6-FR calculations potentials have about the same strength and slope at the small radii and the surface which corresponds to the small overlap or low-density region. We noted also that the folding potentials calculated using the Pauli correlation effect (M3Y-P) are much shallower than the other folded potentials at small distances. The reason is that the Pauli correlation effect is one of medium effect as the same as the DDM3Y-FR and CDM3Y6-FR interactions. Also, we concluded that the Pauli correlation effect is consequently much more repulsive effective interaction.

On the other hand, when we compared the present results with the previous analyses, we found that the DDM3Y-FR, CDM3Y6-FR, and DDM3Y-ZR potentials predictions fit the data better than those produced by the DF M3Y potential but with the same N_R (0.53 to 0.74) obtained by the previous studies. At the same time, the value of N_R is approximately close to one, when we used the M3Y NN interactions with the Pauli correlation effect (M3Y-P). The success of our potentials in the description of the data is equivalent to that obtained with microscopic potentials based on the M3Y, DFC, and with phenomenological potentials. The extracted reaction cross sections are quite consistent with those obtained by the previous studies using microscopic potentials based upon different versions of the effective NN interactions and phenomenological potentials. We can conclude that our results are insensitive to strength parameters of the imaginary potential at near- and sub-barrier energies for $^{32}S + ^{24}Mg$ reactions. It is worthwhile to point out that the present analysis shows an additional confirmation of the ability of the M3Y-P DF potential to successfully reproduce the measured elastic scattering and reaction cross sections for HI systems.

In general, from the present analysis, we can extract interesting conclusion. The real DDM3Y-FR and CDM3Y6-FR DF potentials with finite-exchange terms and density dependence have successfully reproduced the elastic scattering differential cross-section data for HI reactions at near- and sub-barrier energies. The anomaly remains, and the different corrections are used only to produce a uniform shift of the renormalization coefficient.

Finally, the effect of Pauli correlation has been observed clearly when the energy of the projectile increases. So, it would be much more satisfactory if our studies considered the effect of Pauli correlation on the light heavy ions as $^{16}O + ^{16}O$ at high energies.

References

1. M. El-Azab Farid, M.A. Hassanain, Nucl. Phys. A **678**, 39 (2000)
2. M. El-Azab Farid and M. A. Hassanain, Nucl. Phys. A **697**, 183 (2001)
3. M. El-Azab Farid and M. A. Hassanain, Eur. Phys. J. A **19**, 231 (2004)
4. M.A. Hassanain, A.A. Ibraheem, M. El-Azab Farid, Phys. Rev. C: Nucl. Phys. **77**, 034601 (2008)
5. M.A. Hassanain, Int. J. Mod. Phys. E **20**, 1–16 (2011)
6. M.A. Hassanain, Prog. Theor. Phys. **126**, 2 (2011)
7. G.R. Satchler, W.G. Love, Phys. Rep. **55**, 183 (1979)
8. G. Bertsch, J. Borysowicz, H. McManus, W.G. Love, Nucl. Phys. A **284**, 399 (1977)
9. N. Anantaraman, H. Toki, F.F. Bertsch, Nucl. Phys. A **398**, 269 (1983)
10. L.C. Chamon, D. Pereira, M.S. Hussein, M.A.C. Ribeiro, D. Galetti, Phys. Rev. Lett. **79**, 5218 (1997)
11. L.C. Chamon, D. Pereira, M.S. Hussein, Phys. Rev. C: Nucl. Phys. **58**, 576 (1998)
12. L.C. Chamon, B.V. Carlson, L.R. Gasques, D. Pereira, C. De Conti, M.A.G. Alvarez, M.S. Hussein, M.A. Candido Ribeiro, E.S. Rossi Jr., C.P. Silva, Phys. Rev. C: Nucl. Phys. **C66**, 4610 (2002)
13. L.C. Chamon, B.V. Carlson, L.R. Gasques, D. Pereira, C. De Conti, M.A.G. Alvarez, M.S. Hussein, M.A. Candido Ribeiro, E.S. Rossi Jr., C.P. Silva, Braz. J. Phys. **33**(2), (2003)
14. M.Y.H. Farag, M.Y.M. Hassan, Czechoslov. J. Phys. **53**, 473 (2003)
15. M.Y. H. Farag and M.Y.M. Hassan, Czechoslov. J. Phys. **54**, 633 (2004)
16. M.Y.H. Farag, Eur. Phys J. A **12**, 405 (2001)
17. M. El-Azab Farid, Phys. Rev. C **65**, 067303 (2002)
18. J.C. Pacheco, B. Bilwes, F. Sanchez, J.A. Ruiz, J. Diaz, J.L. Ferrero, D. Kadi- Hanifi, Nucl. Phys. A **588**, 537 (1995)
19. H.H. Gutbrod, M. Blann, W.G. Winn, Nucl. Phys. A **213**, 285 (1973)
20. D.T. Khoa, W. von Oertzen, H.G. Bohlen, Phys. Rev. C: Nucl. Phys. **49**, 1652 (1994)
21. D.T. Khoa, W. von Oertzen, Phys. Lett. B **342**, 6 (1995)
22. D.T. Khoa, W. von Oertzen, H.G. Bohlen, G. Bartnitzky, H. Clement, Y. Sugiyama, B. Gebauer, A.N. Ostrowski, T.H. Wilpert, M. Wilpert, C. Langner, Phys. Rev. Lett. **74**, 34 (1995)
23. D.T. Khoa, G.R. Satchler, W. von Oertzen, Phys. Rev. C: Nucl. Phys. **51**, 2069 (1995)
24. D.T. Khoa, G.R. Satchler, W. von Oertzen, Phys. Rev. C: Nucl. Phys. **56**, 954 (1997)
25. D.T. Khoa, G.R. Satchler, Nucl. Phys. A **668**, 3 (2000)
26. D.T. Khoa, W. von Oertzen, H.G. Bohlen, F. Nuoffer, Nucl. Phys. A **672**, 387 (2000)
27. B. Bilwes, R. Bilwes, L. Stuttge, F. Ballester, J. Diaz, J.L. Ferrero, C. Roldan, F. Sanchez, Nucl. Phys. A **473**, 353 (1987)
28. B. Bilwes, R. Bilwes, J. Dlaz, J.L. Ferrero, J.C. Pacheco, J.A. Ruiz, Nucl. Phys. A **484**, 174 (1988)
29. J. Diaz, J.L. Ferrero, J.A. Ruiz, B. Bilwes, R. Bilwes, Nucl. Phys. A **494**, 311 (1989)
30. D.T. Khoa, W. von Oertzen, Phys. Lett. B **304**, 8 (1993)
31. D.T. Khoa, Phys. Rev. C: Nucl. Phys. **63**, 034007 (2001)
32. G.R. Satchler, *Introduction to nuclear reactions* (Oxford Univ. Press, Oxford, 1990)
33. P.J. Moffa, C.B. Dover, J.P. Vary, Phys. Rev. C: Nucl. Phys. **16**, 1857 (1977)
34. M. El-Azab Farid, G.R. Satchler, Nucl. Phys. A **438**, 525 (1985)
35. L.W. Townsend, J.W. Wilson, H.B. Bidasams, Can. J. Phys. **60**, 1514 (1982)
36. L.W. Townsend, Can. J. Phys. **61**, 93 (1983)
37. B. Sinha, Phys. Rep. **20**, 1 (1975)
38. X. Campi, A. Bouysoy, Phys. Lett. B **73**, 263 (1978)
39. J.W. Negele, Phys. Rev. C: Nucl. Phys. **1**, 1260 (1970)
40. A.K. Chaudhuri, D.N. Basu, B. Sinha, Nucl. Phys. A **439**, 415 (1985)
41. A.K. Chaudhuri, B. Sinha, Nucl. Phys. A **455**, 169 (1986)
42. D.T. Khoa, Nucl. Phys. A **484**, 376 (1988)
43. D.T. Khoa, A. Faessler, N. Ohtsuka, J. Phys. G: Nucl. Phys. **16**, 1253 (1990)
44. A.M. Kobos, B.A. Brown, P.E. Hodgson, G.R. Satchler, A. Budxanowski, Nucl. Phys. A **384**, 65 (1982)
45. A.M. Kobos, B.A. Brown, P.E. Hodgson, R. Lindsay, G.R. Satchler, Nucl. Phys. A **425**, 205 (1984)
46. M. A. Hassanain (unpublished)
47. Dao T. Khoa (unpublished)
48. N. M. Clarke (unpublished)
49. Y. Kucuk, I. Boztosun, Nucl. Phys. A **764**, 160 (2006)